Mechanics Research Communications 38 (2011) 471–476

Contents lists available at ScienceDirect

Mechanics Research Communications

journal homepage: www.elsevier.com/locate/mechrescom

A meshless collocation method for the plane problems of functionally graded material beams and plates using the DRK interpolation

Chih-Ping Wu *, Shih-Wei Yang, Yung-Ming Wang, Hsuan-Teh Hu

Department of Civil Engineering, National Cheng Kung University, Tainan 70101, Taiwan, ROC

ARTICLE INFO

Article history:
Received 23 July 2010
Received in revised form 20 April 2011
Available online 27 May 2011

Keywords:
Meshless methods
Collocation
Reproducing kernel
Interpolation
FGM
Plates

ABSTRACT

A meshless collocation method is developed for the static analysis of plane problems of functionally graded (FG) elastic beams and plates under transverse mechanical loads using the differential reproducing kernel (DRK) interpolation, in which the DRK interpolant is constructed by the randomly distributed nodes. A point collocation method based on this DRK interpolation is developed for the plane stress and strain problems of homogeneous and FG elastic beams and plates. It is shown that the present DRK interpolation-based collocation method is indeed a truly meshless approach with excellent accuracy and has a fast convergence rate.

1. Introduction

The development and application of efficient meshless methods have attracted considerable attention in recent decades. The meshless methods in the published literature can be classified into two major categories, namely the collocation-based and Galerkin-based methods, for solving the strong- and weak-forms of the problems considered, respectively. The former includes the smooth particle hydrodynamics (Monaghan, 1988), *h-p* cloud (Liszka et al., 1996), point interpolation collocation (Liu and Gu, 2001), least-squares collocation (Zhang et al., 2001), and finite point (Õnate et al., 2001) methods, and the later includes the reproducing kernel (RK) particle (Liu et al., 1995), moving least square (Liu et al., 1997; Li and Liu, 1996), element-free Galerkin (EFG) (Belytschko et al., 1994), meshless local Petrov–Galerkin (MLPG) (Atluri and Zhu, 1998), and local integral equation (LIE) (Sladek et al., 2006a, 2007) methods. Comprehensive literature surveys of the meshless methods have been undertaken by Atluri and Shen (2002), Belytschko et al. (1994), Li and Liu (2002), and Liu and Gu (2005).

Based on the weak formulation, Sladek et al. (2003, 2005, 2006a,b, 2007, 2008) developed the MLPG and LIE methods for the analyses of elastodynamic, viscoelastic static and thermoelastic problems of solids and plates with FG material properties. They concluded that higher order derivatives occur in governing equations for the above-mentioned problems, that requires more accurate meshless approximation in the strong formulation than in the weak one. In the weak formulation, it is possible to decrease the order of derivatives, and lower order derivatives are more accurately approximated than higher order ones.

This literature review, given below, will focus on the published works dealing with the development and application of the meshless collocation methods using the RK approximants and interpolants. Liu et al. (1995) proposed an RK particle method for numerical analysis of partial differential equations, in which the continuous RK functions were developed by satisfying a set of the reproducing conditions, and a point collocation method based on these was presented by Aluru (2000). Another point collocation method, based on the fast moving least-square reproducing kernel approximation, was developed by Kim and Kim (2003) and Lee et al. (2008), in which a scheme of approximating derivatives was proposed, and it was successfully applied to solve the Poisson and Stokes problems. Li and Liu (1998) developed a synchronized RK interpolation method, for which the convergence rate of the higher-order derivatives of the shape functions can be turned to that of the shape function itself. Li and Liu (1999a,b) proposed a method of RK hierarchical partition of unity, in which a class of basic wavelet functions was introduced to achieve the partitioning.

Wu et al. (2008) developed a differential reproducing kernel (DRK) approximation-based collocation method for the quasi-3D analysis of multilayered piezoelectric plates and FG magneto-electro-elastic shells. The novelty of this DRK approximation is in the determination of the shape functions of derivatives of the

* Corresponding author. Tel.: +886 6 2757575;fax: +886 6 2370804.
E-mail address: cpwu@mail.ncku.edu.tw (C.-P. Wu).

0093-6413/$ – see front matter © 2011 Elsevier Ltd. All rights reserved.
doi:10.1016/j.mechrescom.2011.05.008

RK approximants, which are obtained using a set of differential reproducing conditions without directly differentiating the approximants, as is necessary in the conventional approach. However, the DRK approximation method mentioned above is just like other conventional RK approximation methods, in that the shape functions of RK approximants at each sampling node do not possess the Kronecker delta properties, and this may cause difficulties when the essential boundary conditions are imposed in the implementation of the meshless methods. In order to overcome this inconvenience, Wang et al. (2010) presented a meshless collocation method based on the DKR interpolation instead of the DRK approximation, where the shape function of the DRK interpolant at each sampling node is separated into a primitive function satisfying the Kronecker delta properties and an enrichment function constituting the reproducing conditions. In this paper, the DRK interpolation-based collocation method is extended to the plane elasticity problems of FG elastic beams and plates under transverse mechanical loads, in which an elliptic, rather than a circular, influence zone is used for the weight function at each sampling node, and some critical points with regard to the implementation of this method are studied, such as the optimal support size and the highest order of the basis functions.

2. The DRK interpolation

2.1. The DRK interpolant

It is assumed that there are n_p discrete nodes randomly selected and located at $\boldsymbol{x} = \boldsymbol{x}_1, \boldsymbol{x}_2, \ldots, \boldsymbol{x}_{n_p}$, respectively, in the physical domain $\boldsymbol{\Omega}$, in which $\boldsymbol{x}_I = (x_I, y_I)$, $I = 1, 2, \ldots, n_p$. The DRK interpolant $u^a(\boldsymbol{x})$ of the unknown function $u(\boldsymbol{x})$, $\forall\, \boldsymbol{x} \in \boldsymbol{\Omega}$, is defined as

$$u^a(\boldsymbol{x}) = \sum_{I=1}^{n_p} N_I(\boldsymbol{x}) u_I = \sum_{I=1}^{n_p} [\bar{\phi}_I(\boldsymbol{x}) + \hat{\phi}_I(\boldsymbol{x})] u_I, \tag{1}$$

where $N_I(\boldsymbol{x})$ is the shape function of the DRK interpolant at the sampling node $\boldsymbol{x} = \boldsymbol{x}_I$; u_I is the nodal values of $u^a(\boldsymbol{x})$ at $\boldsymbol{x} = \boldsymbol{x}_I$; $\hat{\phi}_I(\boldsymbol{x})$ ($I = 1, 2, \ldots, n_p$) denote the primitive functions used to introduce the Kronecker delta properties; $\bar{\phi}_I(\boldsymbol{x})$ ($I = 1, 2, \ldots, n_p$) denote the enrichment functions for imposing the nth-order reproducing conditions, and are given by $\bar{\phi}_I(\boldsymbol{x}) = w_a(\boldsymbol{x} - \boldsymbol{x}_I)\mathbf{P}^T(\boldsymbol{x} - \boldsymbol{x}_I)\bar{\mathbf{b}}(\boldsymbol{x})$ in which $\mathbf{P}^T(\boldsymbol{x} - \boldsymbol{x}_I)$ denotes a set of the complete nth-order polynomial functions, $\boldsymbol{P}^T(\boldsymbol{x} - \boldsymbol{x}_I) = \left\lfloor 1, \quad (x - x_I), \quad (y - y_I), \right.$ $\left. (x - x_I)^2, \quad (x - x_I)(y - y_I), \quad (y - y_I)^2, \ldots (x - x_I)^n \right\rfloor$, $\mathbf{b}^T(\boldsymbol{x})$ denotes the undetermined function vector and will be determined by satisfying the reproducing conditions, and $w_a(\boldsymbol{x} - \boldsymbol{x}_I)$ is the weight function centered at $\boldsymbol{x}_I$ with an elliptic support zone.

By selecting the complete nth-order polynomials as the basis functions to be reproduced, we obtain a set of reproducing conditions to determine the undetermined functions of $\bar{b}_i(\boldsymbol{x})$ ($i = 1, 2, \ldots, n_n$) in Eq. (1) in which n_n is the total number of the basis functions and $n_n = (n+1)(n+2)/2$, and these reproducing conditions are given as

$$\sum_{I=1}^{n_p} [\bar{\phi}_I(\boldsymbol{x}) + \hat{\phi}_I(\boldsymbol{x})] x_I^r y_I^s = x^r y^s \quad r + s \le n. \tag{2}$$

Eq. (2) represents n_n, $n_n = (n+1)(n+2)/2$, reproducing conditions, and can be rearranged in the explicit form of

$$r = s = 0: \quad \sum_{I=1}^{n_p} \bar{\phi}_I(\boldsymbol{x}) = 1 - \sum_{I=1}^{n_p} \hat{\phi}_I(\boldsymbol{x}), \tag{3}$$

$$r = 1,\ s = 0: \quad \sum_{I=1}^{n_p} (x - x_I)\bar{\phi}_I(\boldsymbol{x}) = x \sum_{I=1}^{n_p} \bar{\phi}_I(\boldsymbol{x}) - \sum_{I=1}^{n_p} x_I \bar{\phi}_I(\boldsymbol{x}) = 0 - \sum_{I=1}^{n_p} (x - x_I)\hat{\phi}_I(\boldsymbol{x}), \tag{4}$$

$$r = 0,\ s = 1: \quad \sum_{I=1}^{n_p} (y - y_I)\bar{\phi}_I(\boldsymbol{x}) = y \sum_{I=1}^{n_p} \bar{\phi}_I(\boldsymbol{x}) - \sum_{I=1}^{n_p} y_I \bar{\phi}_I(\boldsymbol{x}) = 0 - \sum_{I=1}^{n_p} (y - y_I)\hat{\phi}_I(\boldsymbol{x}), \tag{5}$$

$$r = 2,\ s = 0: \quad \sum_{I=1}^{n_p} (x - x_I)^2 \bar{\phi}_I(\boldsymbol{x}) = x^2 \sum_{I=1}^{n_p} \bar{\phi}_I(\boldsymbol{x}) - 2x \sum_{I=1}^{n_p} x_I \bar{\phi}_I(\boldsymbol{x}) + \sum_{I=1}^{n_p} x_I^2 \bar{\phi}_I(\boldsymbol{x}) = 0 - \sum_{I=1}^{n_p} (x - x_I)^2 \hat{\phi}_I(\boldsymbol{x}), \tag{6}$$

$$\vdots$$

$$r = 0,\ s = n: \quad \sum_{I=1}^{n_p} (y - y_I)^n \bar{\phi}_I(\boldsymbol{x}) = 0 - \sum_{I=1}^{n_p} (y - y_I)^n \hat{\phi}_I(\boldsymbol{x}). \tag{7}$$

The matrix form of the reproducing conditions in Eqs. (3)–(7) is given as

$$\sum_{I=1}^{n_p} \mathbf{P}(\boldsymbol{x} - \boldsymbol{x}_I)\bar{\phi}_I(\boldsymbol{x}) = \mathbf{P}(\mathbf{0}) - \sum_{I=1}^{n_p} \mathbf{P}(\boldsymbol{x} - \boldsymbol{x}_I)\hat{\phi}_I(\boldsymbol{x}), \tag{8}$$

where $\mathbf{P}(\mathbf{0}) = \begin{bmatrix} 1 & 0 & 0 & \cdots & 0 \end{bmatrix}^T$.

Substituting the expression of $\bar{\phi}_I(\boldsymbol{x})$ into the reproducing conditions given in Eq. (8), we may obtain the undetermined function vector $\bar{b}(\boldsymbol{x})$ in the following form:

$$\bar{b}(\boldsymbol{x}) = \mathbf{A}^{-1}(\boldsymbol{x}) \left[\mathbf{P}(\mathbf{0}) - \sum_{I=1}^{n_p} \mathbf{P}(\boldsymbol{x} - \boldsymbol{x}_I)\hat{\phi}_I(\boldsymbol{x}) \right], \tag{9}$$

where $\mathbf{A}(\boldsymbol{x}) = \sum_{I=1}^{n_p} \mathbf{P}(\boldsymbol{x} - \boldsymbol{x}_I) w_a(\boldsymbol{x} - \boldsymbol{x}_I) \mathbf{P}^T(\boldsymbol{x} - \boldsymbol{x}_I)$.

Substituting Eq. (9) into Eq. (1) yields the shape functions of the DRK interpolant in the following form:

$$N_I(\boldsymbol{x}) = \bar{\phi}_I(\boldsymbol{x}) + \hat{\phi}_I(\boldsymbol{x}) \quad (I = 1, 2, \ldots, n_p), \tag{10}$$

where $\bar{\phi}_I(\boldsymbol{x}) = w_a(\boldsymbol{x} - \boldsymbol{x}_I)\mathbf{P}^T(\boldsymbol{x} - \boldsymbol{x}_I)\mathbf{A}^{-1}(\boldsymbol{x}) \left[\mathbf{P}(\mathbf{0}) - \sum_{I=1}^{n_p} \mathbf{P}(\boldsymbol{x} - \boldsymbol{x}_I)\hat{\phi}(\boldsymbol{x}) \right]$.

It is noted from Eq. (10) that the enrichment functions should vanish at all the nodal points (i.e., $\bar{\phi}_I(\boldsymbol{x}_k) = 0$), if we select a set of primitive functions satisfying the Kronecker delta properties (i.e., $\hat{\phi}_I(\boldsymbol{x}_k) = \delta_{Ik}$) with their support sizes not covering any neighboring nodal points, a priori, then the shape functions of the interpolation function will satisfy the Kronecker delta properties (i.e., $N_I(\boldsymbol{x}_k) = \delta_{Ik}$).

2.2. Derivatives of the DRK interpolant

Because the DRK interpolant $u^a(\boldsymbol{x})$ is given in Eq. (1), its first-order derivative with respect to x is expressed as

$$\frac{\partial u^a(\boldsymbol{x})}{\partial x} = \sum_{I=1}^{n_p} N_I^{(x)}(\boldsymbol{x})\, u_I = \sum_{I=1}^{n_p} \left(\bar{\phi}_I^{(x)}(\boldsymbol{x}) + \frac{\partial \hat{\phi}_I(\boldsymbol{x})}{\partial x} \right) u_I, \tag{11}$$

where $N_I^{(x)}(\boldsymbol{x})$ denotes the shape function of the first-order derivative of $u^a(\boldsymbol{x})$ with respect to x; and $\bar{\phi}_I^{(x)}(\boldsymbol{x}) = w_a(\boldsymbol{x}-\boldsymbol{x}_I)\boldsymbol{P}^T(\boldsymbol{x}-\boldsymbol{x}_I)\bar{\boldsymbol{b}}_x(\boldsymbol{x})$, in which $\bar{\boldsymbol{b}}_x(\boldsymbol{x})$ is an undetermined function vector.

The differential reproducing conditions for a set of complete nth-order polynomials are given as

$$\sum_{I=1}^{n_p} \left[\phi_I^{(x)}(\boldsymbol{x}) + \frac{\partial \hat{\phi}_I(\boldsymbol{x})}{\partial x} \right] x_I^r\, y_I^s = r\, x^{r-1}\, y^s \quad r+s \le n. \tag{12}$$

Eq. (12) represents n_n reproducing conditions, and can be rearranged in the matrix form of

$$\sum_{I=1}^{n_p} \mathbf{P}(\boldsymbol{x}-\boldsymbol{x}_I)\bar{\phi}_I^{(x)}(\boldsymbol{x}) = -\mathbf{P}_x(\mathbf{0}) - \sum_{I=1}^{n_p} \mathbf{P}(\boldsymbol{x}-\boldsymbol{x}_I)\frac{\partial \hat{\phi}_I(\boldsymbol{x})}{\partial x}, \tag{13}$$

where $(-1)[\mathbf{P}_x(\mathbf{0})] = -\left.\dfrac{\partial \mathbf{P}(\boldsymbol{x}-\boldsymbol{x}_I)}{\partial x}\right|_{x=x_I} = \begin{bmatrix} 0 & -1 & 0 & \cdots & 0 \end{bmatrix}^T$.

Substituting the expression of $\bar{\phi}_I^{(x)}(\boldsymbol{x})$ given in Eq. (11) into Eq. (13) yields

$$\bar{b}_x(\boldsymbol{x}) = \mathbf{A}^{-1}(\boldsymbol{x}) \left[-\mathbf{P}_x(\mathbf{0}) - \sum_{I=1}^{n_p} \mathbf{P}(\boldsymbol{x}-\boldsymbol{x}_I)\frac{\partial \hat{\phi}_I(\boldsymbol{x})}{\partial x} \right]. \tag{14}$$

Substituting Eq. (14) into Eq. (11) yields the first-order derivative of the DRK interpolant with respect to x in the form of

$$N_I^{(x)}(\boldsymbol{x}) = \bar{\phi}_I^{(x)}(\boldsymbol{x}) + \frac{\partial \hat{\phi}_I(\boldsymbol{x})}{\partial x}, \tag{15}$$

where $\bar{\phi}_I^{(x)}(\boldsymbol{x}) = w_a(\boldsymbol{x}-\boldsymbol{x}_I)\mathbf{P}^T(\boldsymbol{x}-\boldsymbol{x}_I)\mathbf{A}^{-1}(\boldsymbol{x}) \left[-\mathbf{P}_x(\mathbf{0}) - \sum_{I=1}^{n_p} P(\boldsymbol{x}-\boldsymbol{x}_I)\frac{\partial \hat{\phi}_I(\boldsymbol{x})}{\partial x} \right]$.

Carrying out the same derivation process for the higher-order derivatives of $u^a(\boldsymbol{x})$ leads to

$$\frac{\partial^{p+q} u^a(\boldsymbol{x})}{\partial x^p\, \partial y^q} = \sum_{I=1}^{n_p} N_I^{(\overbrace{xx\ldots}^{p}\overbrace{yy\ldots}^{q})}(\boldsymbol{x}) u_I, \tag{16}$$

where $N_I^{(\overbrace{xx\ldots}^{p}\overbrace{yy\ldots}^{q})}(\boldsymbol{x}) = \bar{\phi}_I^{(\overbrace{xx\ldots}^{p}\overbrace{yy\ldots}^{q})}(\boldsymbol{x}) + \frac{\partial^{p+q}\hat{\phi}_I(\boldsymbol{x})}{\partial x^p\, \partial y^q}$,

$$\bar{\phi}_I^{(\overbrace{xx\ldots}^{p}\overbrace{yy\ldots}^{q})}(\boldsymbol{x}) = w_a(\boldsymbol{x}-\boldsymbol{x}_I)\mathbf{P}^T(\boldsymbol{x}-\boldsymbol{x}_I)\mathbf{A}^{-1}(\boldsymbol{x}) \left[(-1)^{p+q}\mathbf{P}_{\underbrace{xx\ldots}_{p}\underbrace{yy\ldots}_{q}}(\mathbf{0}) - \sum_{I=1}^{n_p} \mathbf{P}(\boldsymbol{x}-\boldsymbol{x}_I)\frac{\partial^{p+q}\hat{\phi}_I(\boldsymbol{x})}{\underbrace{\partial xx\ldots}_{p}\,\underbrace{\partial yy\ldots}_{q}} \right],$$

$$\mathbf{P}_{\underbrace{xx\ldots}_{p}\underbrace{yy\ldots}_{q}}(\mathbf{0}) = \left.\frac{\partial^{p+q}\mathbf{P}(\boldsymbol{x}-\boldsymbol{x}_I)}{\partial x^p\, \partial y^q}\right|_{x=x_I}.$$

2.3. Weight functions and the relative L_2 error norm

In implementing the present DRK interpolation, the weight and primitive functions ($w_a(\boldsymbol{x}-\boldsymbol{x}_I)$ and $\hat{\phi}(\boldsymbol{x}-\boldsymbol{x}_I)$) must be selected in advance, and they are given as

Normalized Gaussian function :

$$w_a(s) = \begin{cases} \dfrac{e^{-(s/\alpha)^2} - e^{-(1/\alpha)^2}}{1 - e^{-(1/\alpha)^2}} & \text{for } s \le 1 \\ 0 & \text{for } s > 1 \end{cases}, \tag{17}$$

$$\text{Quartic spline : } \hat{\phi}(s) = \begin{cases} -3s^4 + 8s^3 - 6s^2 + 1 & \text{for } s \le 1 \\ 0 & \text{for } s > 1 \end{cases}, \tag{18}$$

where $s = \sqrt{(x-x_I)^2 + (y-y_I)^2(a_x/a_y)^2}/a_x$ due to the fact that an elliptic influence zone is used in this paper, in which a_x and a_y denote the principal radii of curvature of this elliptic, and the ratio between them is taken to be a constant related to the in-plane dimension of the physical domain considered, for example it is given as $a_x/a_y = L_x/L_y$, for a rectangular domain with an in-plane dimension of $L_x \times L_y$; and the value of α in Eq. (17) is taken to be 0.3, as commonly used in the literature. As Wang et al. (2010) suggested, the normalized Gaussian function is adopted for the weight function in this analysis due to its higher-order continuous property, and the quartic spline function with a support size (either a_x or a_y) which does not cover any neighboring node is used as the primitive function for each sampling point.

The relative L_2 error norm of the strain energy of an elastic body is defined as follows:

$$(L_2)_{\Pi} = \frac{\sqrt{\sum_{I=1}^{n_p} [(\Pi_I)_{num} - (\Pi_I)_{exact}]^2}}{\sqrt{\sum_{I=1}^{n_p} (\Pi_I)_{exact}^2}}, \tag{19}$$

where the subscript Π denotes the strain energy density of an elastic body; and Π is given as $\Pi = (\sigma_x\varepsilon_x + \sigma_y\varepsilon_y + \tau_{xy}\gamma_{xy})/2$ in plane elasticity problems, in which $(\sigma_x, \sigma_y, \tau_{xy})$ and $(\varepsilon_x, \varepsilon_y, \gamma_{xy})$ are the in-plane stress and strain components, respectively.

The convergence rate of the relative error norm is defined as

$$R = \frac{Log_{10}[(L_2)_{i+1}/(L_2)_i]}{Log_{10}[(\Delta x)_{i+1}/(\Delta x)_i]}, \tag{20}$$

where $(\Delta x)_i$ and $(\Delta x)_{i+1}$ are the uniform nodal spacings for the coarse and refined node distributions, respectively.

3. Applications

The present DRK interpolation-based collocation method is applied to some typical plane elasticity problems of solids, which are the static analyses of a deep homogeneous elastic beam under transverse sinusoidal loading and an infinitely long FG elastic plate under cylindrical bending. The governing equations of the plane elasticity in terms of the displacement components in the x and y directions are given as follows:

$$(c_{11}\, u_{,x} + c_{12}\, v_{,y})_{,x} + \left\lfloor c_{33}(u_{,y} + v_{,x}) \right\rfloor_{,y} = 0, \tag{21}$$

$$\left\lfloor c_{33}\,(u_{,y} + v_{,x}) \right\rfloor_{,x} + (c_{12} u_{,x} + c_{22}\, v_{,y})_{,y} = 0, \tag{22}$$

where u and v denote the displacement components in the x and y directions, respectively; and c_{ij} $(i, j = 1, 2, 3)$ are the elastic stiffness coefficients for the isotropic material, which are given as follows:

For plane stress problems,

$$c_{11} = c_{22} = \frac{E}{(1-\upsilon^2)}, \quad c_{12} = \frac{\upsilon E}{(1-\upsilon^2)}, \quad c_{33} = \frac{E}{2(1+\upsilon)};$$

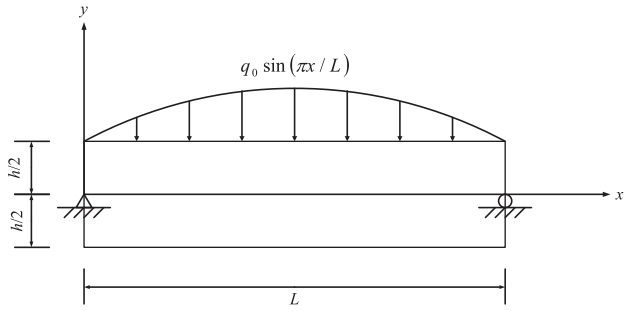

Fig. 1. The configuration and coordinates of the deep beam.

For plane strain problems, $c_{11} = c_{22} = \dfrac{(1-\upsilon)E}{(1+\upsilon)(1-2\upsilon)}$,

$$c_{12} = \frac{\upsilon E}{(1+\upsilon)(1-2\upsilon)}, \quad c_{33} = \frac{E}{2(1+\upsilon)};$$

in which E and υ denote the Young's modulus and Poisson's ratio, respectively, and it is assumed that υ is constant and E a certain function of the thickness coordinate (y) for the FGM beams/plates.

The possible boundary conditions at each point on the boundary edge are

$$\text{either} \quad (c_{11}u_{,x} + c_{12}v_{,y})n_x + c_{33}(u_{,y} + v_{,x})n_y = \hat{t}_x \quad \text{or } u = \hat{u}, \tag{23a}$$

$$\text{either } c_{33}(u_{,y} + v_{,x})n_x + (c_{12}u_{,x} + c_{22}v_{,y})n_y = \hat{t}_y \quad \text{or } v = \hat{v}, \tag{23b}$$

where n_x and n_y are the direction cosines of the unit vector relative to the given coordinates; $\hat{t}_x$ and $\hat{t}_y$ are the traction components; and $\hat{u}$ and $\hat{w}$ are the prescribed displacement components.

3.1. A deep beam under transverse sinusoidal loading

A plane stress problem, which deals with the static behavior of a simply supported, deep homogeneous isotropic beam under transverse sinusoidal loading (i.e., $q = -q_0 \sin(\pi x/L)$, and $q_0 = 1\,\mathrm{KN_t/m^2}$), as shown in Fig. 1, is studied. The thickness (h) and length (L) of the deep beam are 2 m × 8 m, and the Young's modulus and Poisson's ratio are 70 GPa and 0.3, respectively. The boundary conditions at the edges are given as follows:

$$\sigma_x(0,y) = 0 \quad \text{and} \quad \int_{-h/2}^{h/2} \tau_{xy}(0,y)\,dy = -q_0\frac{L}{\pi}, \quad \text{at } x = 0 \quad \text{and} \quad \frac{-h}{2} \le y \le \frac{h}{2}, \tag{24a}$$

$$\sigma_x(L,y) = 0 \quad \text{and} \quad \int_{-h/2}^{h/2} \tau_{xy}(L,y)\,dy = q_0\frac{L}{\pi}, \quad \text{at } x = L \quad \text{and} \quad \frac{-h}{2} \le y \le \frac{h}{2}, \tag{24b}$$

$$\sigma_y\left(x, \frac{h}{2}\right) = -q_0 \sin\left(\frac{\pi x}{L}\right) \quad \text{and} \quad \tau_{xy}\left(x, \frac{h}{2}\right) = 0, \quad \text{at } y = \frac{h}{2} \quad \text{and} \quad 0 \le x \le L, \tag{24c}$$

$$\sigma_y\left(x, \frac{-h}{2}\right) = 0 \quad \text{and} \quad \tau_{xy}\left(x, \frac{-h}{2}\right) = 0, \quad \text{at } y = \frac{-h}{2} \quad \text{and} \quad 0 \le x \le L. \tag{24d}$$

Note that the boundary conditions given in Eqs. (24a) and (24b) do not specify the pointwise distribution of shear stress on the edges of the deep beam, but rather stipulate the resultant condition based on overall problem equilibrium. It is thus necessary to assume a certain through-thickness distribution of the shear stress at two edges ($x = 0$ and L) for which the resultant shear force corresponding to the assumed shear stress should be equivalent to the one given in Eqs. (24a) and (24b), so that the boundary conditions at these edges can be imposed node by node in the implementation of the present collocation method. In order to validate the accuracy and convergence rate of this collocation method, the boundary conditions at the edges of $x = 0$ and $x = L$ given in Eqs. (24a) and (24b) are replaced, as follows:

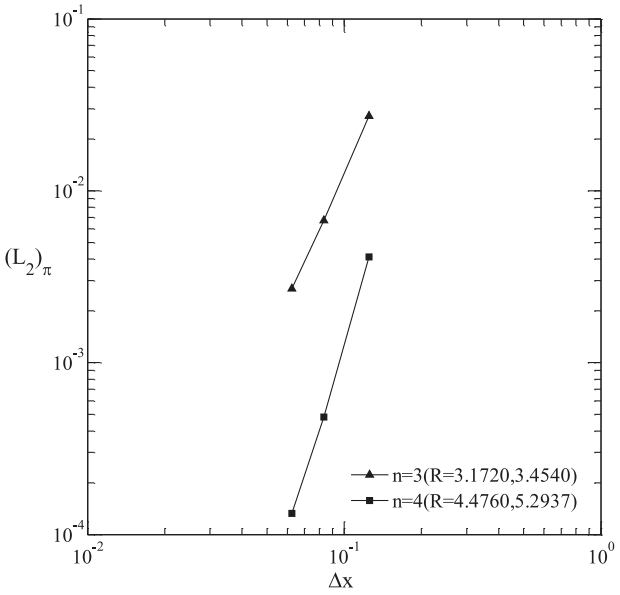

Fig. 2. The convergence rate of $(L_2)_{\Pi}$ of the deep beam.

$$\sigma_x(0,y) = 0 \quad \text{and} \quad \tau_{xy}(0,y) = \hat{\tau}_{xy}(0,y), \quad \text{at } x = 0 \quad \text{and} \quad \frac{-h}{2} \le y \le \frac{h}{2}, \tag{25a}$$

$$\sigma_x(L,y) = 0 \quad \text{and} \quad \tau_{xy}(L,y) = \hat{\tau}_{xy}(L,y), \quad \text{at } x = L \quad \text{and} \quad \frac{-h}{2} \le y \le \frac{h}{2}, \tag{26b}$$

where $\hat{\tau}_{xy}$ is the analytical solution of Timoshenko and Goodier (1970).

Table 1 shows the results for the dimensionless stress and displacement components ($\bar{\sigma}_x$ and $\bar{v}$) induced at the centre of the beam, in which $\bar{\sigma}_x = \sigma_x/q_0$, $\bar{v} = 100h^3 E\,v/(L^4 q_0)$, ($n = 3$, $a_x = 4.1\Delta x$, $a_y = a_x/4$) and ($n = 4$, $a_x = 4.6\Delta x$, $a_y = a_x/4$) are taken, and the regular distributions of 9×9, 11×11, 13×13 and 17×17 nodes are used. It is seen in Table 1 that the solutions converge rapidly, and the relative L_2 error norm of the strain energy of the beam is 0.27% for the 17×17 solution with ($n = 3$, $a_x = 4.1\Delta x$, $a_y = a_x/4$) and 0.013% for the 17×17 solution with ($n = 4$, $a_x = 4.6\Delta x$, $a_y = a_x/4$), as compared with the exact solutions.

Fig. 2 shows the convergence rate (R) of $(L_2)_{\Pi}$ of the beam with $n = 3$ and 4, and the average values of R are 3.31 for $n = 3$ and 4.88 for $n = 4$. The 9×9 and 17×17 solutions of the through-length and -thickness distributions of displacement and stresses, respectively, are presented in Fig. 3, in which $n = 3$. As expected, the displacement solution is a higher-order polynomial through the length coordinate, that of bending stress is linear through the thickness coordinate, and that of shear stress is parabolic. It is also shown that the 17×17 solutions are in excellent agreement with the exact ones.

3.2. An infinitely-long FGM plate under cylindrical bending

A plane strain problem, which deals with the static behavior of a simply-supported, infinitely long FG isotropic plate under the cylindrical bending type of loading ($q = -q_0 \sin(\pi x/L)$, and $q_0 = 1\,\mathrm{N_t/m^2}$), is studied. The plate is made of aluminum (bottom) and alumina (top), for which the Young's modulus obeys a power-law

Table 1
The solutions for the dimensionless displacement and stress components induced at the centre of the beam under a sinusoidally distributed load.

Node-distributions	$(n=3,\ a_x=4.1\Delta x,\ a_y=a_x/4)$			$(n=4,\ a_x=4.6\Delta x,\ a_y=a_x/4)$		
	$\bar{v}(L/2,\ 0)$	$\bar{\sigma}_x(L/2,\ h/2)$	$(L_2)_\pi$	$\bar{v}(L/2,\ 0)$	$\bar{\sigma}_x(L/2,\ h/2)$	$(L_2)_\pi$
9×9	−13.9745	−9.8299	2.73e−02	−14.1602	−9.9697	4.12e−03
11×11	−14.0490	−9.9051	1.27e−02	−14.1289	−9.9599	1.30e−03
13×13	−14.0755	−9.9263	6.72e−03	−14.1163	−9.9569	4.82e−04
17×17	−14.0934	−9.9437	2.70e−03	−14.1088	−9.9560	1.33e−04

Exact solutions: $\bar{v}(L/2,\ 0)=-14.1066$, $\bar{\sigma}_x(L/2,\ h/2)=-9.9568$.

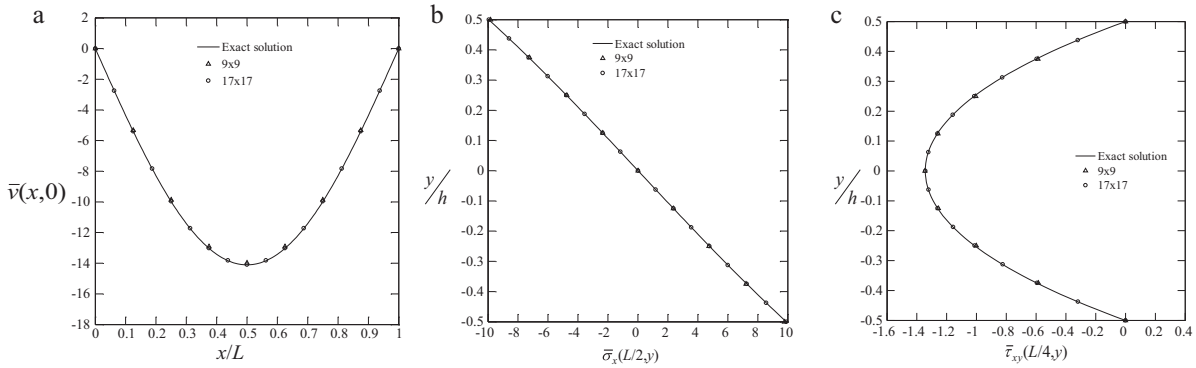

Fig. 3. The through-length and through-thickness distributions of displacement and stress components.

distribution of the volume fractions of the constituents, and the Poisson's ratio remains constant, as given by

$$E(y)=E_m+(E_c-E_m)\left[\frac{(2y+h)}{2h}\right]^{\kappa}\quad \frac{-h}{2}\le y\le\frac{h}{2}, \tag{27}$$

$$\upsilon(y)=0.3\quad \frac{-h}{2}\le y\le\frac{h}{2}, \tag{28}$$

where the subscripts of m and c denote the metal and ceramic materials constituting the bottom and top layers, respectively, $E_m=70$ GPa and $E_c=380$ GPa, and κ is the volume fraction exponent, which are taken to be 0, 1, 5, 10 and ∞, in which when $\kappa=0$ and ∞ this FGM plate will be reduced to a homogeneous plate with $E=E_c$ and $E=E_m$, respectively.

The total thickness and length of the plate are considered to be 2 m × 8 m. The boundary conditions of this simply-supported plate are given as follows:

$$\sigma_x(0,y)=0,\quad w(0,y)=0,\quad \text{at}\,x=0\quad\text{and}\quad \frac{-h}{2}\le y\le\frac{h}{2}, \tag{29a}$$

$$\sigma_x(L,y)=0,\quad w(L,y)=0,\quad \text{at}\,x=L\quad\text{and}\quad \frac{-h}{2}\le y\le\frac{h}{2}, \tag{29b}$$

Table 2
The present solutions of dimensionless displacement and stress components induced at the centre of the beam under a sinusoidally distributed load.

Node-distributions	$\bar{v}(L/2,\ 0)$	$\bar{\sigma}_x(L/2,\ h/2)$	$(L_2)_\pi$	R
9×9	−12.9469	−9.9290	4.73e−03	–
11×11	−12.9582	−9.9512	1.27e−03	–
13×13	−12.9530	−9.9535	6.93e−04	4.74
17×17	−12.9487	−9.9551	3.05e−04	2.85

Exact solutions: $\bar{v}(L/2,\ 0)=-12.9476$, $\bar{\sigma}_x(L/2,\ h/2)=-9.9568$.

and the ones at the top and bottom surfaces of the plate are in the same forms as Eqs. (24c) and (24d), which are commonly used in the literature (Wu and Li, 2010; Wu et al., 2011).

Table 2 shows the results for the dimensionless stress and displacement components ($\bar{\sigma}_x$ and $\bar{v}$) induced at the centre of the plate, in which $\bar{\sigma}_x=\sigma_x/q_0$, $\bar{v}=100h^3E_m\nu/(L^4q_0)$, $n=4$, $a_x=4.6\Delta x$, $a_y=a_x/4$, and the regular distributions of 9×9, 11×11, 13×13 and 17×17 nodes are used. It is seen in Table 2 that the solutions converge rapidly, and the relative L_2 error norm of the strain energy of the plate is 0.03% for the 17×17 solution as compared with the exact solutions obtained using the modified Pagano method (Wu et al., 2010).

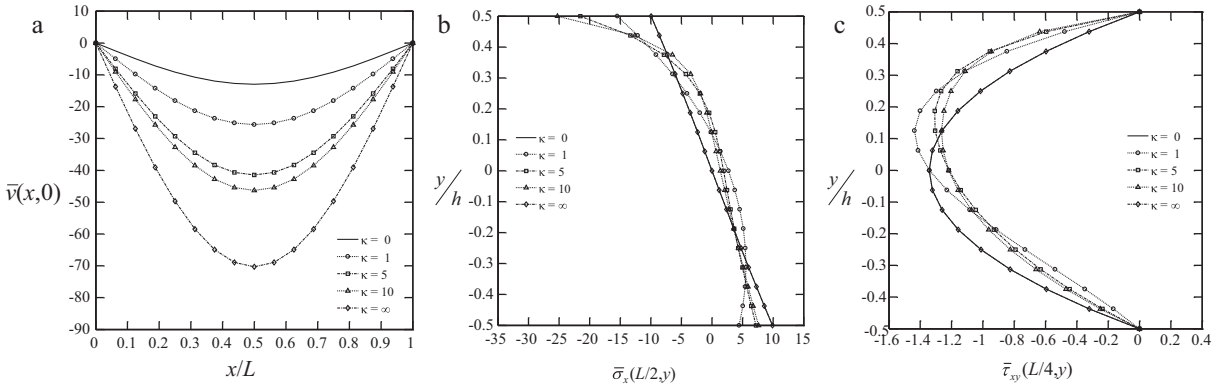

Fig. 4. The variations of the through-length distributions of displacement and through-thickness distributions of stress components with the volume fraction exponent κ.

Fig. 4 shows the variations of the through-length distributions of displacement and through-thickness distributions of stress components with κ, in which $\bar{\sigma}_x = \sigma_x/q_0$, $\bar{\tau}_{xy} = \tau_{xy}/q_0$, $\bar{v} = 100h^3 E_c v/(L^4 q_0)$, and the regular distribution of 17×17 nodes, $n = 4$, $a_x = 4.6\Delta x$ and $a_z/a_x = 1/4$ are taken. It is seen in Fig. 4 that the through-thickness distributions of stress components induced in the FG plates ($\kappa \neq 0$ or ∞) are quite different from those in the homogeneous plate. The distributions of the in-plane normal stresses appear to be higher-order polynomials through the thickness coordinate of the FG plates, while they are linear functions through the thickness coordinate of the homogeneous plates. The through-thickness distributions of the in-plane shear stresses induced in the FG plates appear to be higher-order polynomials with the maximum value occurring at the upper portion of the plate, while they are parabolic functions with the maximum value in the middle surface of the homogeneous plates. The deflection of the FG plates increases when the volume fraction exponent becomes larger; meanwhile, the overall performance of the plate becomes softer.

4. Conclusions

In this paper, we extended the DRK interpolation-based collocation method to the plane elasticity analysis of homogeneous and FGM beams and plates under mechanical loads. Two benchmark problems, which are Timoshenko and Goodier's plane stress problem of a deep homogeneous beam and Pagano's plane strain problem of an infinite-long homogeneous plate, were used to validate the accuracy and convergence rate of the present collocation method. Subsequently, this method was extensively applied to the analysis of FGM plates. In the illustrated examples, it is shown that the present method using 17×17 nodes with $n = 4$, $a_x = 4.6\Delta x$, $a_y = a_x/4$ may lead to satisfactory results with a fast convergence rate, in which the $(L_2)_{\Pi}$ error norm is 0.013% and the convergence rate (R) is about 4.9 in the plane stress case, and $(L_2)_{\Pi}$ is 0.03% and R is about 3.8 in the plane strain case. Moreover, the through-thickness distributions of normal stress components induced in the FG plates ($\kappa \neq 0$ or ∞) are different from those in the homogeneous plate. These distributions appear to be higher-order polynomials through the thickness coordinate of the FG plates, while they are linear functions through the thickness coordinate of the homogeneous plates.

Acknowledgment

This work was supported by the National Science Council of Republic of China through Grant NSC 97-2221-E006-128-MY3.

References

Aluru, N.R., 2000. A point collocation method based on reproducing kernel approximations. Int. J. Numer. Methods Eng. 47, 1083–1121.
Atluri, S.N., Shen, S., 2002. The Meshless Local Petrov–Galerkin (MLPG) Method. Tech Science Press, Encino, CA.
Atluri, S.N., Zhu, T., 1998. A new meshless local Petrov–Galerkin (MLPG) approach in computational mechanics. Comput. Mech. 22, 117–127.
Belytschko, T., Lu, Y.Y., Gu, L., 1994. Element-free Galerkin methods. Int. J. Numer. Methods Eng. 37, 229–256.
Kim, D.W., Kim, Y., 2003. Point collocation methods using the fast moving least-square reproducing kernel approximation. Int. J. Numer. Methods Eng. 56, 1445–1464.
Lee, C., Kim, D.W., Park, S.H., Kim, H.K., Im, C.H., Jung, H.K., 2008. Point collocation mesh-free using FMLSRKM for solving axisymmetric Laplace equation. IEEE Trans. Magn. 44, 1234–1237.
Li, S., Liu, W.K., 1996. Moving least-square reproducing kernel method (II) Fourier analysis. Comput. Methods Appl. Mech. Eng. 139, 159–193.
Li, S., Liu, W.K., 1998. Synchronized reproducing kernel interpolant via multiple wavelet expansion. Comput. Mech. 21, 28–47.
Li, S., Liu, W.K., 1999a. Reproducing kernel hierarchical partition of unity. Part I – formulation and theory. Int. J. Numer. Methods Eng. 45, 251–288.
Li, S., Liu, W.K., 1999b. Reproducing kernel hierarchical partition of unity. Part II – applications. Int. J. Numer. Methods Eng. 45, 289–317.
Li, S., Liu, W.K., 2002. Meshfree and particle methods and their applications. Appl. Mech. Rev. 55, 1–34.
Liu, W.K., Jun, S., Zhang, Y.F., 1995. Reproducing kernel particle methods. Int. J. Numer. Methods Eng. 20, 1081–1106.
Liu, G.R., Gu, Y.T., 2001. A point interpolation method for two-dimensional solids. Int. J. Numer. Methods Eng. 50, 937–951.
Liu, G.R., Gu, Y.T., 2005. An Introduction to Meshfree Methods and Their Programming. Springer, The Netherlands.
Liu, W.K., Li, S., Belytschko, T., 1997. Moving least-square reproducing kernel methods (I) methodology and convergence. Comput. Methods Appl. Mech. Eng. 143, 113–154.
Liszka, T.J., Duarte, C.A.M., Tworzydlo, W.W., 1996. *hp*-meshless cloud method. Comput. Methods Appl. Mech. Eng. 139, 263–288.
Monaghan, J.J., 1988. An introduction to SPH. Comput. Phys. Commun. 48, 89–96.
Õnate, E., Perazzo, F., Miquel, J., 2001. A finite point method for elasticity problems. Comput. Struct. 79, 2151–2163.
Sladek, J., Sladek, V., Hellmich, Ch., Eberhardsteiner, J., 2007. Analysis of thick functionally graded plates by local integral equation method. Commun. Numer. Methods Eng. 23, 733–754.
Sladek, J., Sladek, V., Solek, P., Wen, P.H., Atluri, S.N., 2008. Thermal analysis of Reissner–Mindlin shallow shells with the FGM properties by the MLPG. Comput. Model. Eng. Sci. 30, 77–97.
Sladek, J., Sladek, V., Zhang, Ch., 2003. Application of meshless local Petrov–Galerkin (MLPG) method to elastodynamic problems in continuously nonhomogeneous solids. Comput. Model. Eng. Sci. 4, 637–648.
Sladek, J., Sladek, V., Zhang, Ch., 2005. An advanced numerical method for computing elastodynamic fracture parameters in functionally graded materials. Comput. Mater. Sci. 32, 532–543.
Sladek, J., Sladek, V., Zhang, Ch., Schanz, M., 2006a. Meshless local Petrov–Galerkin method for continuously nonhomogeneous linear viscoelastic solids. Comput. Mech. 37, 279–289.
Sladek, V., Sladek, J., Zhang, Ch., 2006b. A comparative study of meshless approximations in local integral equation method. Comput. Mater. Continua 4, 177–188.
Timoshenko, S.P., Goodier, J.N., 1970. Theory of Elasticity. McGraw-Hill, New York.
Wang, Y.M., Chen, S.M., Wu, C.P., 2010. A meshless collocation method based on the differential reproducing kernel interpolation. Comput. Mech. 45, 585–606.
Wu, C.P., Chen, S.J., Chiu, K.H., 2010. Three-dimensional static behavior of functionally graded magneto-electro-elastic plates using the modified Pagano method. Mech. Res. Commun. 37, 54–60.
Wu, C.P., Chiu, K.H., Wang, Y.M., 2008. A meshfree DRK-based collocation method for the coupled analysis of functionally graded magneto-electro-elastic shells and plates. Comput. Model. Eng. Sci. 35, 181–214.
Wu, C.P., Chiu, K.H., Wang, Y.M., 2011. RMVT-based meshless collocation and element-free Galerkin methods for the quasi-3D analysis of multilayered composite and FGM plates. Compos. Struct. 93, 923–943.
Wu, C.P., Li, H.Y., 2010. The RMVT- and PVD-based finite layer methods for the three-dimensional analysis of multilayered composite and FGM plates. Compos. Struct. 92, 2476–2496.
Zhang, X., Liu, X.H., Song, K.Z., Lu, M.W., 2001. Least-squares collocation meshless method. Int. J. Numer. Methods Eng. 51, 1089–1100.